Research Article

Field Measurement of Wind Speeds and Wind-Induced Responses atop the Shanghai World Financial Center under Normal Climate Conditions

Yong Quan, Shuai Wang, Ming Gu, and Jun Kuang

State Key Laboratory of Disaster Reduction in Civil Engineering, Tongji University, Shanghai 200092, China

Correspondence should be addressed to Ming Gu; minggu@tongji.edu.cn

Field measurement data on wind velocities and wind-induced acceleration responses at the top of the 492 m high Shanghai World Financial Center (SWFC) under normal climate conditions are studied. Characteristics of the mean wind speeds and turbulence intensities, gust factors, power spectral densities, and turbulence integral scales of the fluctuating wind speed are analyzed in different observation time intervals. Power spectral densities of wind-induced acceleration are also investigated. The basic natural frequencies and structural damping ratios of the building are identified based on Hilbert-Huang transform method and random decrement method. The field measurement results of wind-induced responses of the SWFC are finally compared with those from the corresponding high-frequency force balance wind tunnel test study.

1. Introduction

Field measurement of wind velocities and wind-induced responses is an essential aspect of wind engineering. In 1960, a field measurement study on mean wind speed at different heights and time intervals was conducted by Durst [1], who also proposed an empirical formula for different terrain categories. A long-term observation of wind speeds and wind directions with ultrasonic anemometers in Tokyo and Yokohama was performed by Choi [2] and Kato et al. [3]. Several databases on local wind characteristics, for example, the offshore observation databases in Canada and the United Kingdom [4, 5] and the Froya database in Norway [6, 7], were established successively with field measurement data. The characteristics of the mean and fluctuating wind velocity of typhoon Muifa were analyzed by An et al. [8] through field measurement at the top of the Shanghai World Financial Center. The field measurement data of the wind-induced responses at the top of a 254 m high bridge tower was researched by Larose et al. [9] and compared with the corresponding wind tunnel test study results in frequency domain. The dynamic characteristics of a 200 m high building were identified from its field measured wind-induced vibration data by Li et al. [10], and then the correlation between

structural damping and acceleration responses was discussed. Field measurements of the strong wind characteristics and wind-induced responses at the 384 m high Shenzhen Diwang Mansion and the 420.5 m high Shanghai Jin Mao Tower were conducted by Xu and Zhan [11] and Li et al. [12], respectively, and relevant empirical formulas were fitted. Field measured acceleration responses under strong winds at the 391 m high Guangzhou Citic Tower and the 450 m high Guangzhou West Tower were shown by Fu et al. [13, 14] and compared with the corresponding wind tunnel test. Bai et al. [15] studied the wind velocity, acceleration responses, and base bending strains on parts of a transmission tower. Yi et al. [16] and Li et al. [17] applied GPS technology to field measurement of high-rise structures and studied the displacement responses.

The previous studies on the field measured wind speeds and wind-induced responses were mainly focused on typhoon climate conditions, while those under normal climate conditions were barely found. Based on the wind speed and wind-induced acceleration responses measured by the structural health monitoring system (SHMS) installed on the SWFC, the mean and fluctuating wind speeds at a level near 500 m under normal climate conditions are thus analyzed in the present study. The maximum wind speeds
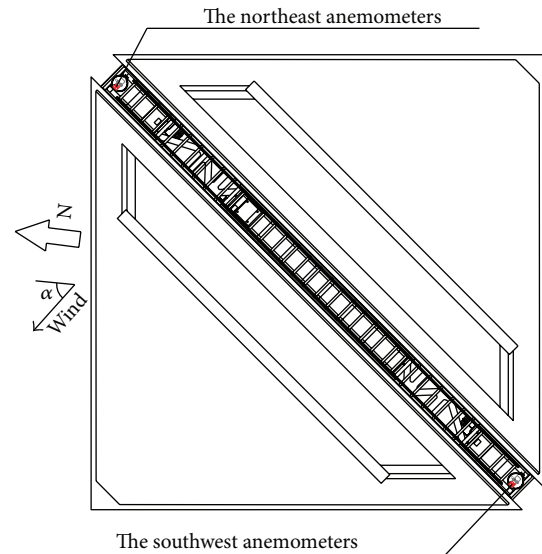
Figure 1: Panorama of SWFC.

Figure 2: Sketch of location of the anemometers.

and the turbulence characteristics for different observation time intervals are discussed. Frequency domain and time-frequency domain analysis of the field measured acceleration responses at the topmost part of the SWFC are also conducted. The dynamics of the building are identified with random decrement method (RDM). The wind-induced acceleration responses from the field measurement are compared with those from the corresponding high-frequency force balance (HFFB) wind tunnel test study. Some conclusions are drawn based on the results.

2. Field Measurement Profile

Figure 1 presents the structural health monitoring system installed in the SWFC, which mainly consists of a wind velocity monitoring system and a structural vibration monitoring system. The wind velocity monitoring system is installed on the northeast and southwest end of the top of the building at a level of 495 m high from the ground (Figure 2). As shown in Figure 3, each side has a Windmaster Pro triaxial ultrasonic anemometer (Gill Co. Ltd, UK). The distance between the two sites of instruments is 72 m. The x-, y-, and z-axes of the anemometer face the north, west, and upward direction, respectively (Figure 4). The wind angle increases along the counterclockwise direction; thus, the measured wind velocity is $0°$ for the south wind and $90°$ for the east wind. Since they are exposed outdoors, the anemometers might be influenced by the climate like rainfall and temperature. The equipment used here has a permissible rainfall less than 300 mm/hr, and the operating temperature is between -40 and $70°$. Thus, the data collection is reliable under normal climate conditions. The measuring range of the anemometer is from 0.01 m/s to 65 m/s. The maximum dynamic response frequency is 40 Hz and the actual sampling frequency is 10 Hz. All the data are collected in real time and stored by using the CR1000 data collection system (Campbell Co. Ltd, USA). In order to prevent the anemometers from being struck by lightning,

Figure 3: Windmaster Pro ultrasonic anemometer.

the anemometers are installed on the beam and fixed on the lightning rod with a flange on each side of the topmost part of the building. Meanwhile, the anemometers are several meters higher than the top of the building to reduce the effects of the building itself, and CFD method was used to identify its effective angles.

Computational fluid dynamics simulation of the wind field around the target building shows that the mean and fluctuating wind speeds approaching the building are influenced by the building itself. However, the influences are negligible when the included angle between the approaching wind and the y-axis of the building is smaller than $15°$ (Figure 5), and those angles are defined as the effective wind angle. Effective wind angle ranges at the northeast and southwest ends are $120°$ to $150°$ and $300°$ to $330°$, respectively. The following analyzed samples are those whose 10 min mean wind speeds
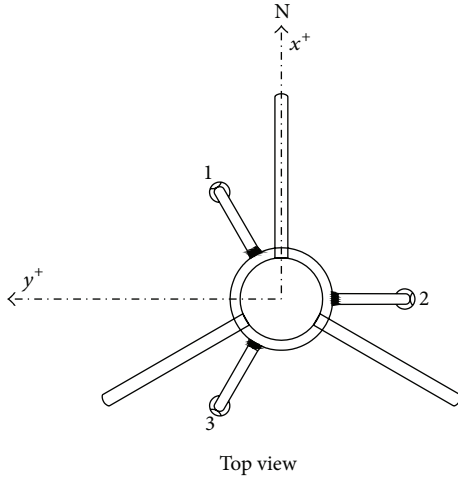
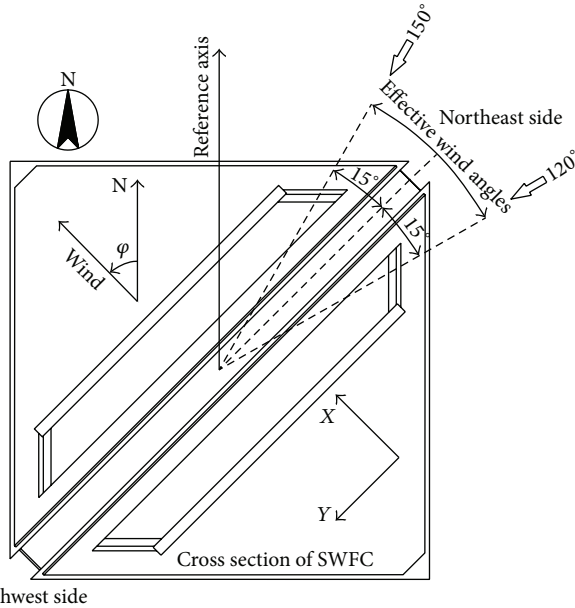Figure 4: Definition of x- and y-axes of the anemometer.

Figure 5: Sketch of axes directions of the building, effective range of wind angles, and definition of wind angles.

are relatively large (over 8 m/s) and wind angles are in the effective wind angle ranges.

The acceleration data are measured by the acceleration sensors installed on the 98th floor of the building (475 m). The acceleration sensors are SLJ-100 balance accelerometer produced by China Earthquake Administration. The basic frequency of the accelerometer is 100 Hz, the measurement range is ±2 g, and the frequency band is 0–100 Hz. The two horizontal normal axes of the sensors are parallel to the body axes of the building (Figure 5). Vibration signals are simultaneously measured from the three orthogonal directions by the sensors. Two different groups of wind-induced responses data with a length of 10 min are selected for further analysis. In those two data groups, the mean wind

speed and the corresponding mean wind angle are 16.33 m/s, 139° and 9.48 m/s, 123°, respectively. Apparently, the mean wind angles fall in the effective wind angle range at the northeast end.

3. Characteristics of Wind Speed

The characteristics of the measured mean and fluctuating wind speeds are analyzed in this section. The wind velocity samples are shown at first. Then, the mean wind speeds under different average time intervals are analyzed. The turbulence intensity, gust factors, and turbulence scales of the fluctuating wind speeds are also discussed.

3.1. Mean Wind Speed. Three orthogonal components of wind speed, $u_x(t)$, $u_y(t)$, and $u_z(t)$, are measured simultaneously with the ultrasonic anemometers from the three directions of the x-, y-, and z-axes, respectively. Ignoring the vertical component, $u_z(t)$, the mean wind speeds, U, and directions, ϕ, are calculated through the vector splitting method as follows:

$$U = \sqrt{\overline{u_x(t)}^2 + \overline{u_y(t)}^2},$$

$$\cos(\phi) = \frac{\overline{u_x(t)}}{U}, \qquad \sin(\phi) = \frac{\overline{u_y(t)}}{U}. \tag{1}$$

The longitudinal and lateral fluctuating components, $u(t)$ and $v(t)$, are calculated with the following formula, respectively:

$$u(t) = u_x(t)\cos\phi + u_y(t)\sin\phi - U,$$

$$v(t) = -u_x(t)\sin\phi + u_y(t)\cos\phi. \tag{2}$$

The analyzed samples are collected from the anemometers at the southwest and northeast ends of the SWFC rooftop (Table 1).

Figure 6 shows the maximum values of mean wind speeds in 1 hr with the durations of 3 s, 10 min, and 1 hr, respectively, and the mean wind angles with a duration of 1 hr. The mean wind angle has no apparent change within the analytical time intervals. The maximum values of mean wind speeds within 1 hr decrease with the increase of the durations, but the maximum 10 min wind speeds within 1 hr are close to the mean wind speed of 1 hr.

Figures 7 and 8 show the relationship between the maximum 10 min mean wind speeds within 1 hr and the 1 hr mean wind speed, as well as that between the maximum 3 s mean wind speeds within 10 min and the 10 min mean wind speeds, respectively. The figures also show a linear fitting in which the length of the error bar in Figure 7 represents the standard deviation, and the fitting demonstrates a good result. As shown in Figure 7, the ratio of the maximum 10 min mean wind speeds within 1 hr and the 1 hr mean speed is approximately 1.04. In most cases, the standard deviation of the maximum 10 min mean wind speeds within 1 hr does not exceed 1 m/s. In Figure 8, the correlation between the

TABLE 1: Record of measured samples.

Location	Date	Recording time	Recording duration (min)	The maximum 10 min mean wind speed (m/s)
Southwest side	February 13, 2009	4:50:00 to 10:49:59	360	21.78
	December 9, 2008	0:00:00 to 9:59:59	600	14.37
Northeast side	February 15, 2009	14:00:00 to 23:59:59	600	15.17
	November 16, 2009	14:00:00 to 17:59:59	240	16.36
	November 9 and 10, 2009	22:20:00 (November 9) to 6:19:59 (November 10)	480	16.97
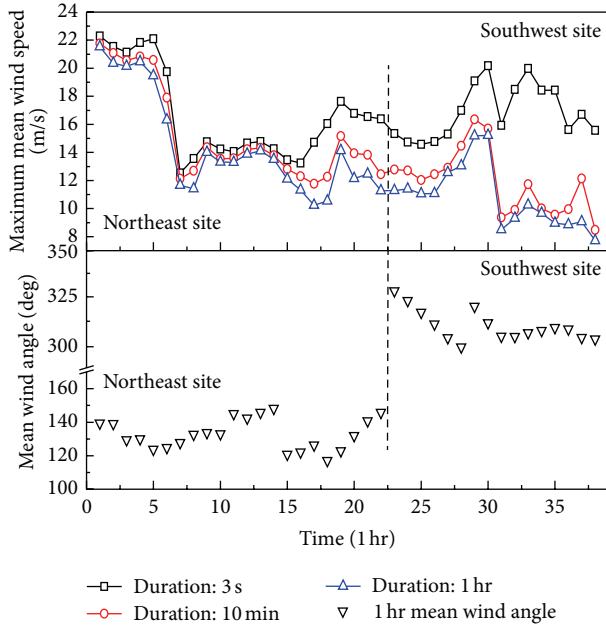
FIGURE 6: Maximum mean wind speeds in 1 hr for different durations and 1 hr mean wind directions.

FIGURE 7: Maximum 10 mean wind speeds versus 1 hr mean wind speeds.

maximum 3 s mean wind speeds within 10 min (instant maximum wind speed) and the 10 min mean wind speeds can be expressed as $y = 0.85x + 4.5$.

3.2. Fluctuating Wind Speeds

3.2.1. Turbulence Intensity and Gust Factor. Turbulence intensity is defined as the ratio of the standard deviation and the mean values of the approaching wind speeds. The analyzed time interval is 10 min (all average time intervals mentioned subsequently are 10 min, unless specified otherwise). The turbulence intensity is calculated as follows:

$$I_i = \frac{\sigma_i}{U} \quad (i = u, v), \tag{3}$$

where σ_i is the standard deviation of the fluctuating wind speeds; u and v represent the longitudinal and lateral components of the fluctuating wind speeds, respectively.
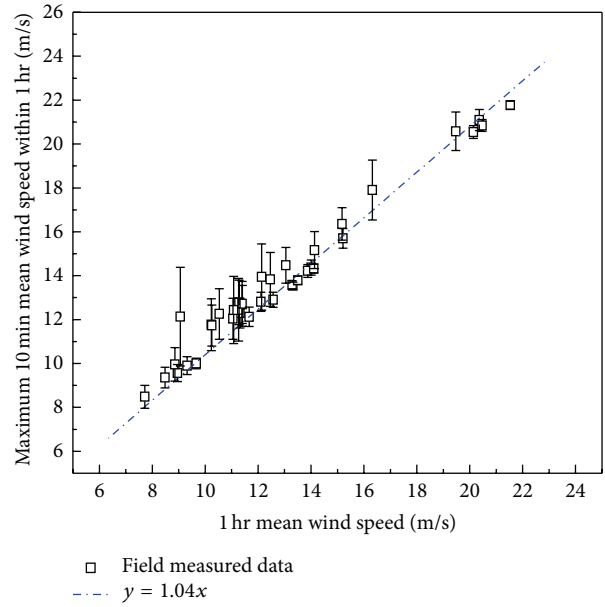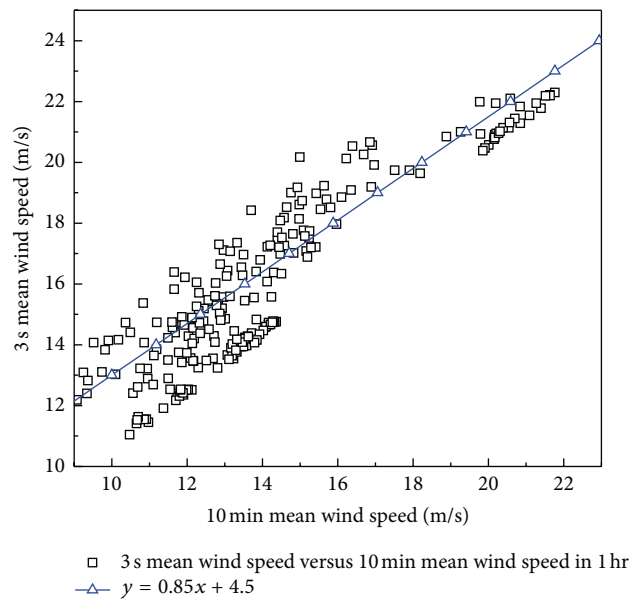

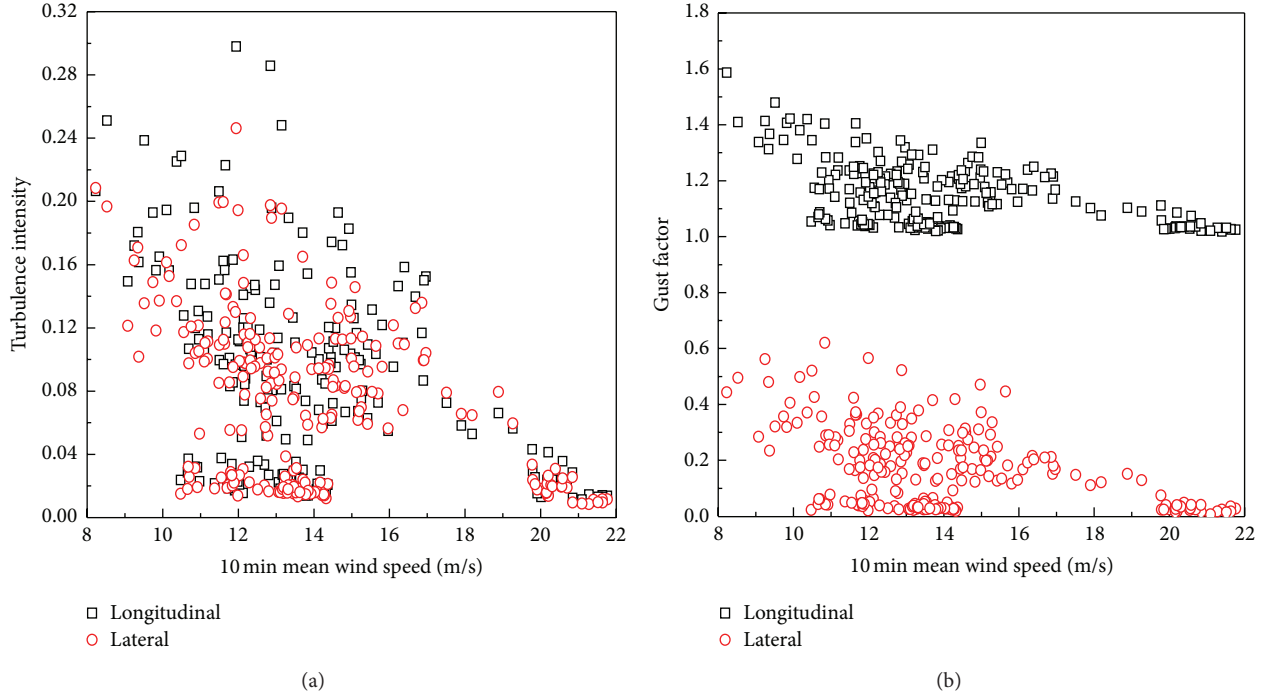FIGURE 8: Maximum 3 s mean wind speeds versus 10 min mean wind speeds.

FIGURE 9: Relationships among turbulence intensities, gust factors, and 10 min mean wind speeds. (a) Turbulence intensities versus mean wind speeds and (b) gust factors versus mean wind speeds.

Gust factor is defined as the ratio of the maximum wind speed within the gust duration, t_g, and the 10 min mean wind speeds U, which can be expressed as

$$G_u\left(t_g\right) = 1 + \frac{\max\left(\overline{u\left(t_g\right)}\right)}{U}, \qquad G_v\left(t_g\right) = \frac{\max\left(\overline{v\left(t_g\right)}\right)}{U}, \tag{4}$$

where $\max(\overline{u(t_g)})$ and $\max(\overline{v(t_g)})$ represent the maximum mean wind speeds of the longitudinal and lateral fluctuating wind speeds, respectively, within the gust duration time $t_g(s)$ during the observation time interval.

Figures 9(a) and 9(b) illustrate the relationships between turbulence intensities and the 10 min mean wind speeds as well as between the gust factors and the 10 min mean wind speeds, respectively. The longitudinal and lateral turbulence intensities both decrease as the mean wind speeds increase (Figure 9(a)). The longitudinal turbulence intensity is in $[0.01, 0.30]$ and the mean value is 0.085. The lateral turbulence intensity is in $[0.01, 0.25]$ and the mean value is 0.075. The ratio of those two values is $\overline{I}_u : \overline{I}_v = 1 : 0.88$. The longitudinal turbulence intensity recommended by AIJ [18] for the same terrain category (V type) and the same height (495 m) is 0.11 and that based on the Chinese load code [19] is 0.12. As shown in Figure 9(b), the longitudinal and lateral gust factors both decrease as the 10 min mean wind speeds increase. Regulations of turbulence intensity and gust factors were also found by Fu et al. [13] through field measurement of a 391 m high-rise building in south China under typhoon condition. Then, the gust factors remain almost the same after

the mean wind speed reaches approximately 20 m/s. When the gust duration time t_g is equal to 3 s, the longitudinal gust factor $\overline{G}_u$ is in $[1.02, 1.59]$ and the mean value is 1.15; the lateral gust factor $\overline{G}_v$ is in $[0.01, 0.62]$ and the mean value is 0.17, $\overline{G}_u : \overline{G}_v = 1 : 0.15$.

Figure 10 shows the correlation between the longitudinal gust factor and the turbulence intensity as well as between the lateral gust factor and the turbulence intensity for a gust duration time of $t_g = 3$ s. The longitudinal and lateral gust factors both increase as the turbulence intensity increases. A linear fitting is shown for the relationship between the turbulence intensity and the gust factor. Then, based on a previous study [20], a nonlinear fitting is used in accordance with the following formula:

$$G_u\left(t_g\right) = 1 + k_1 \times I_u^{k_2} \quad \ln\left(\frac{T}{t_g}\right), \tag{5}$$

where T represents the mean time interval. Choi [21] defined T as 1 hr and suggested that $k_1 = 0.62$ and $k_2 = 1.27$. As shown in Figure 10, the linear fitting relations between the longitudinal gust factors and turbulence intensity as well as between the lateral gust factors, and turbulence intensity are $G_u = 1 + 1.6\,I_u$ and $G_v = 2.4\,I_v$, respectively. The results of the linear and nonlinear fitting are almost similar, which implies that the gust factor and turbulence intensity have a linear relationship. By comparing the measurement results, the empirical formula proposed by Choi [21], as well as the linear and nonlinear fitting, the measured results of the gust factors and the results from the said empirical formula are relatively close when the turbulence intensity is smaller than
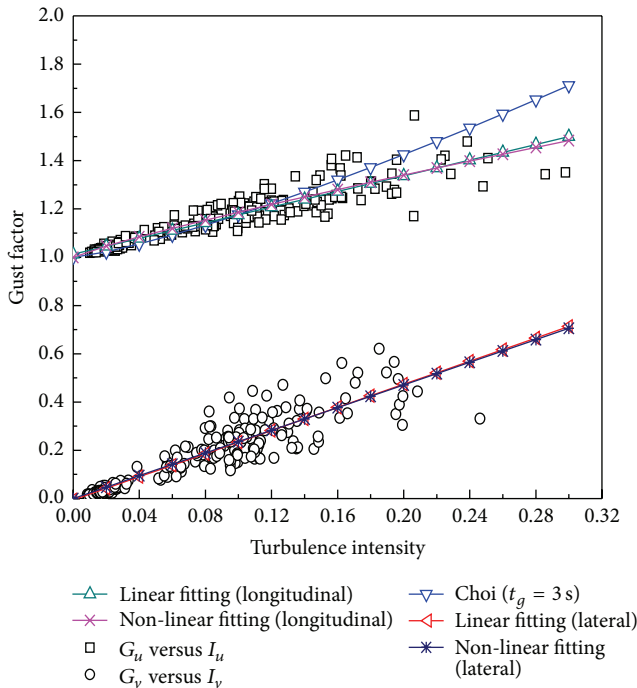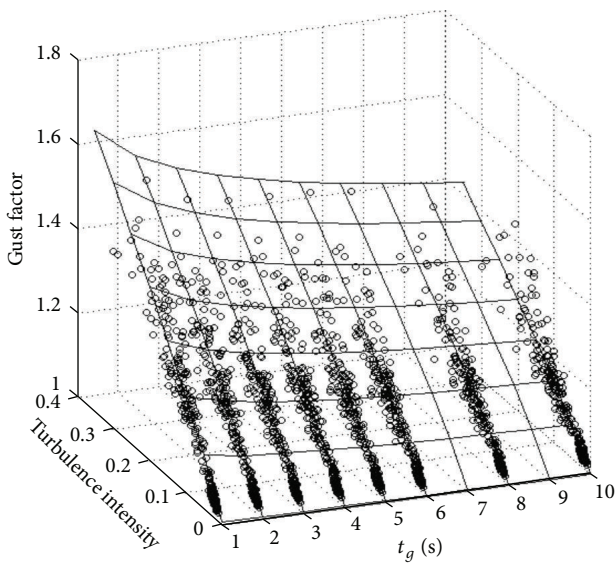
FIGURE 10: Turbulence intensities versus gust factors.

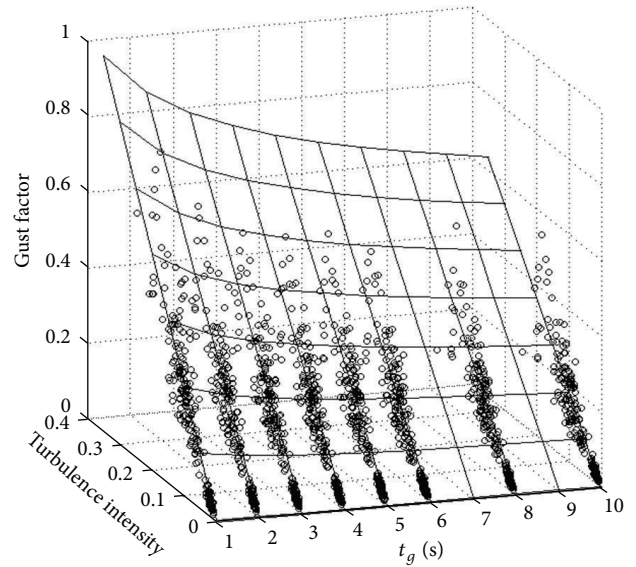FIGURE 11: Correlations between longitudinal gust factors and turbulence intensities in various durations.

FIGURE 12: Correlations between lateral gust factors and turbulence intensities in various durations.
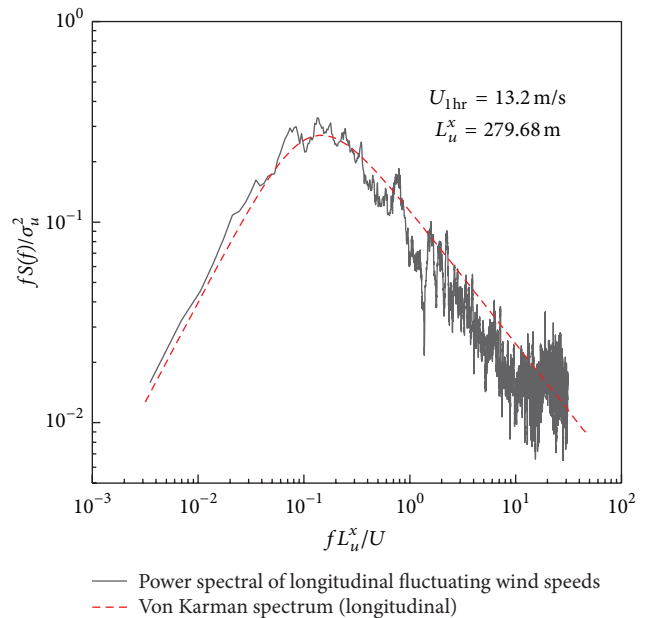
FIGURE 13: PSD of longitudinal fluctuating wind speeds.

0.16. When the turbulence intensity is over 0.16, the measured gust factors are smaller than the calculated ones.

Figures 11 and 12 show the correlation between gust factors and turbulence intensities in various duration times for longitudinal and lateral components of the approaching wind, respectively. Both figures adopt three-dimensional coordinates to show the longitudinal and lateral measured results with hollow round dots. The nonlinear fitting results of formula (5) are also shown in those figures with solid lines. The fitting result of the relationship between the longitudinal gust factors and the turbulence intensities is $G_u = 1 + 0.26 I_u^{0.87} \ln(600/t_g)$. The fitting result of the relationship between the lateral gust factors and turbulence intensities is $G_v = 0.44 I_v \ln(600/t_g)$. When turbulence intensities remain constant, the gust factors decline as the gust duration time t_g increases.

3.2.2. The Power Spectral Density of Fluctuating Wind Speeds. Figures 13 and 14 show the power spectral densities of the longitudinal and lateral fluctuating wind speeds of the field measurement, which is almost matched with the von Karman spectra. However, not all power spectral densities
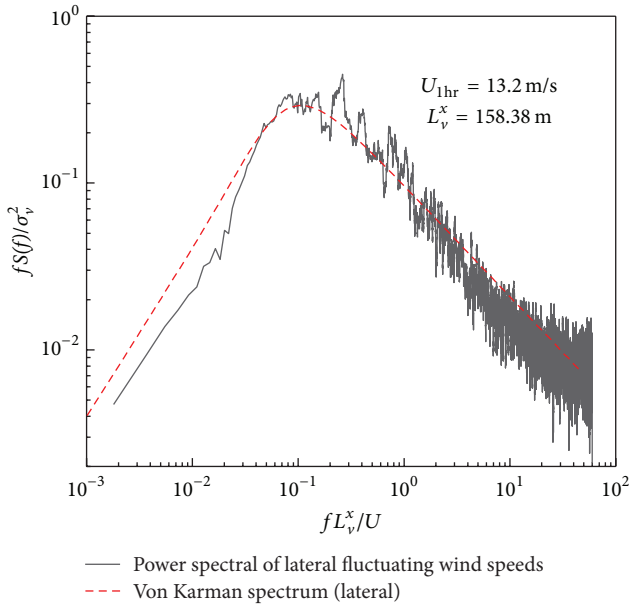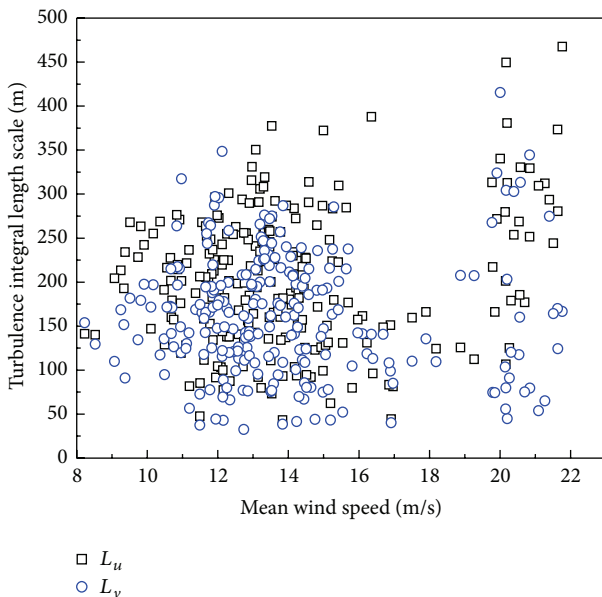
FIGURE 14: PSD of lateral fluctuating wind speeds.

FIGURE 15: Turbulence integral scales versus 10 min mean wind speeds.

of measured fluctuating wind speeds are in accordance with the von Karman spectra, particularly if the mean wind speeds are over 20 m/s. In the power spectral densities of the fluctuating wind speed, both longitudinal and lateral components at high frequency severely deviate from the von Karman spectra and exhibit an uptrend characteristic. Similar phenomenon that power spectral densities match well with the von Karman spectrum at low wind speeds and are uptrend at high wind speeds was also found in the research of Fu et al. [14] at a 450 m high-rise building in south China. The deviation and uptrend characteristic may be caused by

the nonstationary original data. Since fast Fourier transform (FFT) is effective only for stationary data, the power spectral density determined through FFT method cannot reflect the overall characteristics of the original data.

3.2.3. Turbulence Integral Scale. The turbulence integral scale can be expressed as follows:

$$L_i^x = \frac{US_i(0)}{2\sigma_i^2} \quad (i = u, v, w),\tag{6}$$

where $S_i(0)$ is the value that corresponds to the power spectral density of the u, v, and w components of approaching wind speed for a frequency of 0.

Figure 15 shows the relationship between turbulence integral scales and the 10 min mean wind speeds for longitudinal and lateral components of approaching wind. Longitudinal and lateral turbulence integral scales have an increasing trend as the mean wind speeds increase. This trend was also found by Li et al. [10] in the typhoon measurement on the top of Jin Mao building, which is close to SWFC. The mean values of the longitudinal and lateral turbulence integral scales are $\overline{L}_u^x \approx 200$ m and $\overline{L}_v^x \approx 160$ m, respectively. Thus, $\overline{L}_u^x : \overline{L}_v^x = 1 : 0.8$.

4. Acceleration Response of the Building in Normal Climate Wind and Identification of Dynamic Parameters

The time histories and the power spectral densities of the acceleration responses for strong wind in normal climate are discussed at first in this section. Then, time-frequency analysis is conducted with the Hilbert-Huang transform (HHT) method. The dynamic characteristics of the building, that is, basic mode frequency and structural damping ratio, are identified by using the random decrement method. The dynamic characteristics identified from various methods are compared with one another and with the finite element analysis results. Finally, the acceleration responses from the field measurement are analyzed and compared with those from the corresponding wind tunnel test.

4.1. Time History of Acceleration Response. Figures 16 and 17 show the time histories of acceleration responses with particular wind speeds. The lateral wind-induced accelerations (X direction) are significantly larger than the longitudinal ones (Y direction). As shown in Figure 16, both lateral and longitudinal acceleration responses are relatively slight during the first 5 min, but the lateral responses increase sharply in the last 5 min. According to wind velocity records, the increase may be caused by the difference of the wind directions between the first and last 5 min. During the first 5 min, the included angle between the approaching wind and the y-axis of the building is 7°. However, it is 0° in the last 5 min when the vibration in the X direction (lateral direction) is stronger.

In another record of wind-induced acceleration responses as shown in Figure 17, there is no apparent difference between
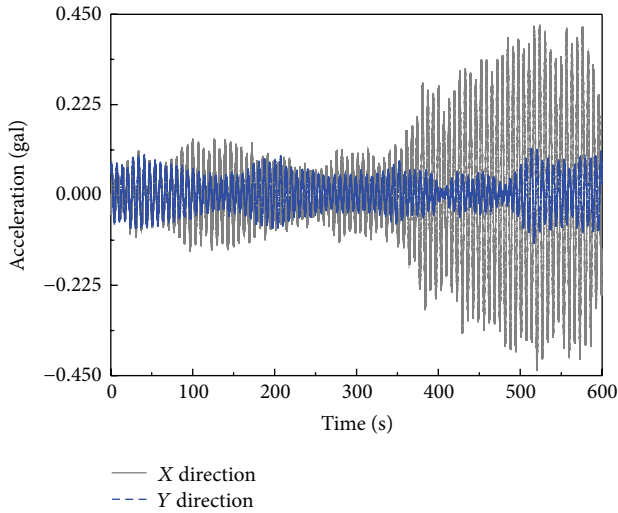
FIGURE 16: Time histories of acceleration responses with a 9.48 m/s wind speed.
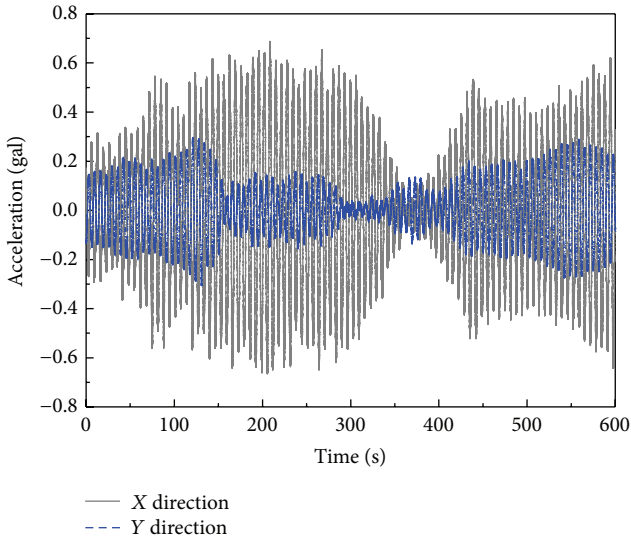

FIGURE 17: Time histories of acceleration responses with 16.33 m/s wind speed.

FIGURE 18: PSD of acceleration responses in X direction with 16.33 m/s wind speed.

FIGURE 19: PSD of acceleration responses in Y direction with 16.33 m/s wind speed.

FIGURE 20: PSD of acceleration responses in X direction with 9.48 m/s wind speed.

the first and last 5 min. Both mean wind speeds and wind directions during the two time intervals have no obvious change.

4.2. Power Spectral Density of Acceleration Response. Figures 18, 19, 20, and 21 present the power spectral densities of the measured acceleration responses in X and Y directions on the 98th floor of the building. The wind-induced vibrations are mainly contributed by the vibrations of the basic modes in structural X and Y directions. The natural vibration frequencies of those two basic modes are close to each other. For example, when the wind speed is 16.33 m/s, the natural vibration frequencies in X and Y directions identified from the power spectral densities are 0.154 Hz and 0.153 Hz, respectively. The responses of the several high-order modes
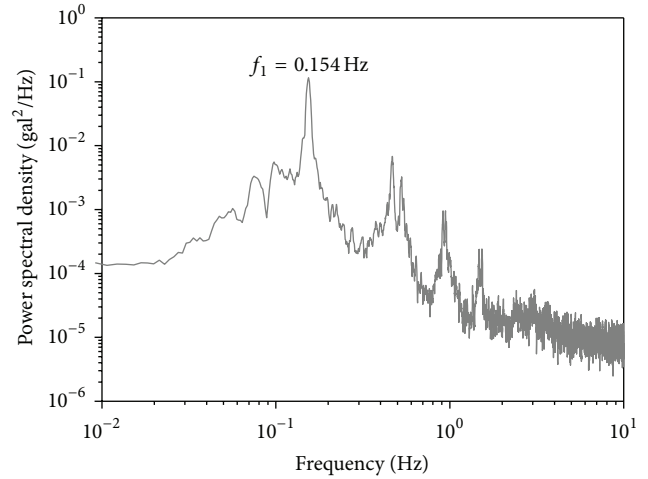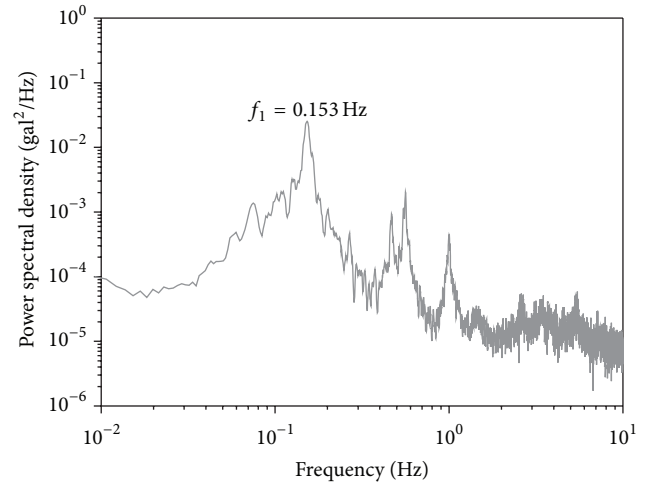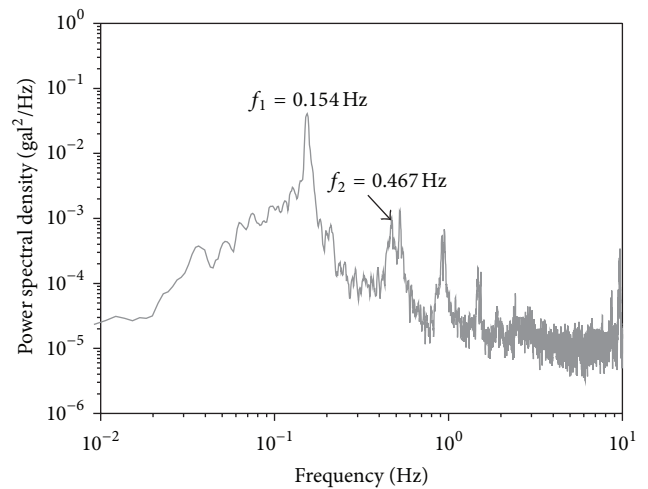
Table 2: Natural vibration frequency of SWFC (Hz).

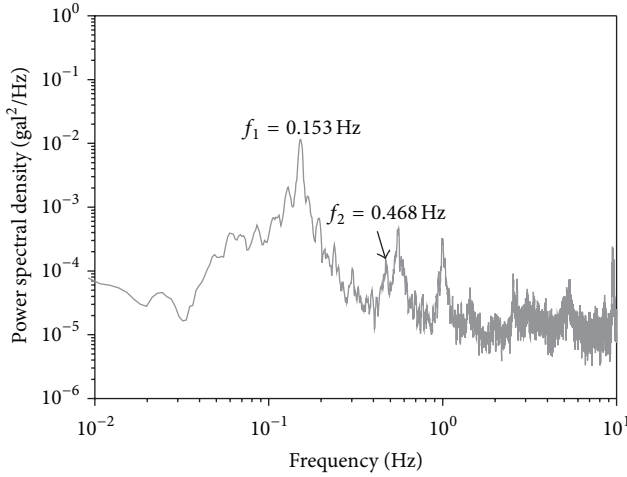| Mode	Finite element method	Measured results		
		FFT method	HHT method	RDM method
First-order bending in Y direction	0.146	0.153	0.152	0.153
First-order bending in X direction	0.153	0.154	0.152	0.155
Second-order bending in X direction	0.465	0.467	0.468	—
Second-order bending in Y direction	0.481	0.468	0.469	—

Figure 21: PSD of acceleration responses in Y direction with 9.48 m/s wind speed.

are perceptible in the power spectral densities, while they are negligible because of the significance of contributions from the basic modes.

4.3. Time-Frequency Analysis of Acceleration Response. Time-frequency analysis of the acceleration responses is conducted on several periods with the HHT method [22]. Based on the HHT analysis, the measured record of acceleration responses corresponding to the fastest 10 min mean wind speed (16.33 m/s) is picked out for the following analysis. Empirical mode decomposition (Figures 22 and 23) is conducted at first. The intrinsic mode functions (IMF) of the first six orders have narrow ranges and high-frequency components but have narrow ranges and low-frequency components in the eleventh to thirteenth orders. Figure 24 shows that the original signals match well with the superposition of IMF in the eighth to tenth orders. Figure 25 indicates that in the low-frequency domain, the power spectral densities of the superimposed IMF in the eighth to tenth orders almost match those of the original data. The matched power spectral densities can effectively reflect the frequency domain characteristics in the first five orders of the building. When the frequency is over 2 Hz, the difference is more apparent because the high-frequency component is filtrated by the IMFs of the eighth to tenth orders.

Figure 26 shows the time-frequency series of acceleration responses. The Hilbert-Huang marginal spectra of acceleration signal in the field measurement are presented in Figure 27. The basic mode frequency in the X direction is 0.152 Hz and 0.468 Hz for the second mode.

4.4. Identification of Dynamic Structural Characteristics in Time Domain. The random decrement method (RDM) [23], a time averaged method, is adopted to identify the natural frequencies and structural damping ratios of the basic mode in X and Y directions of the building.

Figures 28 and 29 show the identified results of the basic natural frequencies and damping ratios in X and Y directions versus the intercepting threshold values. The basic natural frequencies in X and Y directions are 0.155 Hz and 0.153 Hz, respectively, which change hardly with the increase of the intercepting threshold values. When the intercepting thresholds reach a certain value, the damping ratios are almost constant. The values in X and Y directions fluctuate at approximately 2.4% and 1.6%, respectively. The difference of those two values may be attributed to the dissimilar foundation in X and Y directions, which may be caused by the construction of the Shanghai Center Building located in the southwest side of the target building. Therefore, the soil-structure interaction changes the wind-induced responses of SWFC [24] and thus affects the identification of its damping ratios.

Finite element model was established in a former seismic review of SWFC. The profile and vibration mode in Y and X directions of that model are shown in Figure 30. The translational vibration modes of the first two orders according to finite element analysis are in the Y and X directions, and the corresponding basic mode frequencies are 0.146 Hz and 0.153 Hz [25]. Table 2 lists the results of the finite element analysis and this field measurement. The natural frequencies of the first two orders identified by the power spectral density, HHT marginal spectra, and RDM match the natural frequencies from the finite element analysis.

5. Comparison between Field Measured Wind-Induced Responses and Those from HFFB Wind Tunnel Test Study

The Boundary Layer Wind Tunnel Laboratory at the University of Western Ontario, Canada, once conducted a wind tunnel test on SWFC by using the HFFB technology [26]. The laboratory defined two test cases as the present one and the
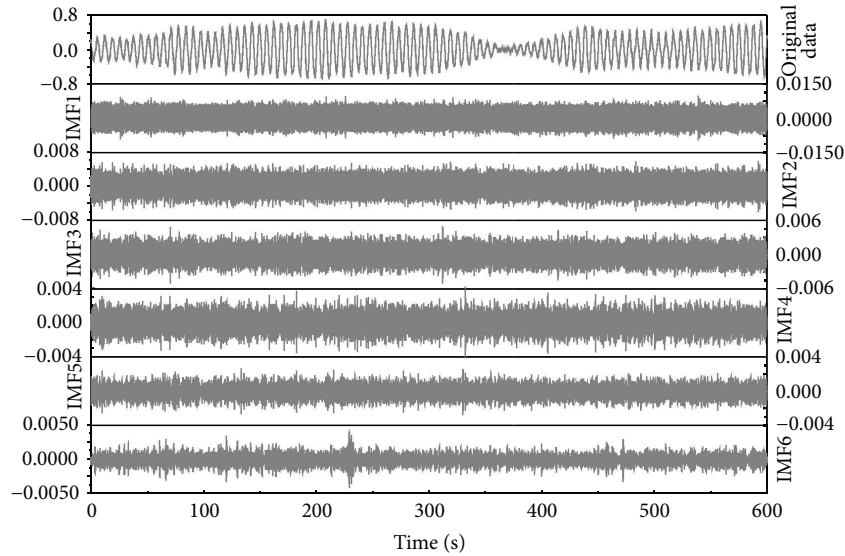
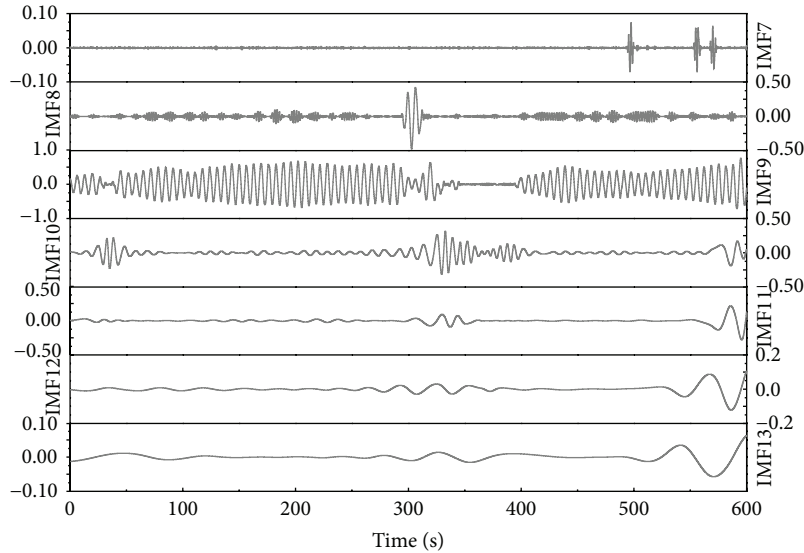FIGURE 22: IMFs of the first to sixth orders.

FIGURE 23: IMFs of the seventh to thirteenth orders.

future one, which are named the first and second environmental conditions, respectively. The first one simulated the environment when SWFC was being built, and the second one added some new high-rise buildings in plan at that time. Particularly, the main distinction between these two test cases is that the second one considered the "future" existence of the Shanghai Center Building, which was designed to be 400 m at that time.

The field measured data are the responses from the 98th floor of the building (approximately 475 m). However, the data from the wind tunnel test study are the responses at the top of the building (492 m). For comparison, the former ones are converted to the top of the building according to the mode and direction. The lengths of field measured acceleration data adopted for the comparison close to 10 min. The mean wind

speeds and wind angles are obtained as shown in Table 3. The wind angles for the wind-induced responses are mostly in the range of northeast effective wind angle range ($120°$ to $150°$); therefore, the interference from the target building itself on the mean wind speeds can be ignored. When the wind tunnel test data are used to calculate the wind-induced responses, the damping ratios for the basic modes in X and Y directions are assumed to be 2.4% and 1.6%, respectively. Since the vibration mode along the height is not strictly linear, hypothesis of a linear distribution and modification of the tested base moment are therefore conducted to calculate the response.

When the mean wind speeds are small, the wind-induced responses in X and Y directions (lateral and longitudinal directions) generally match the measured results
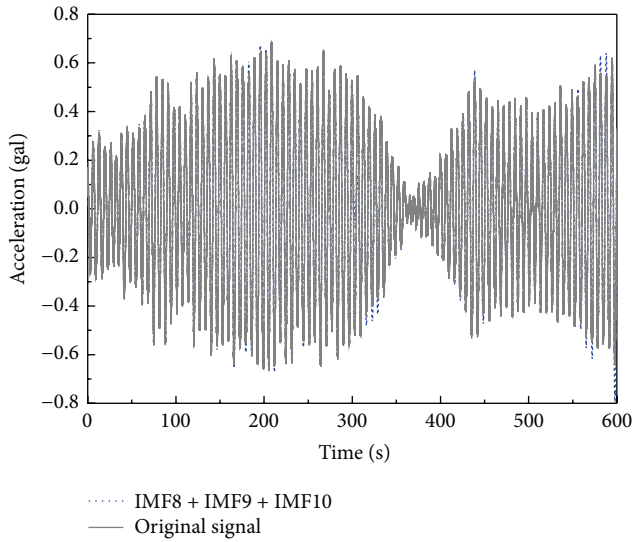
FIGURE 24: Comparison between the original signal and the super-position of IMFs in the eighth to tenth orders.
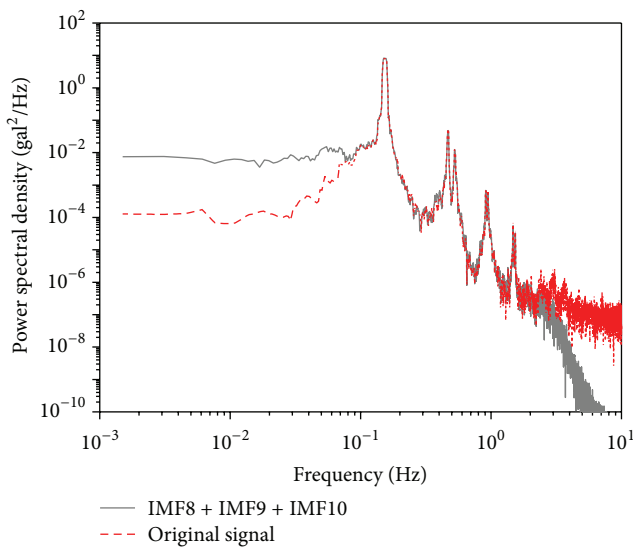

FIGURE 25: PSD of the original signal and superposition of IMFs in the eighth to tenth orders.
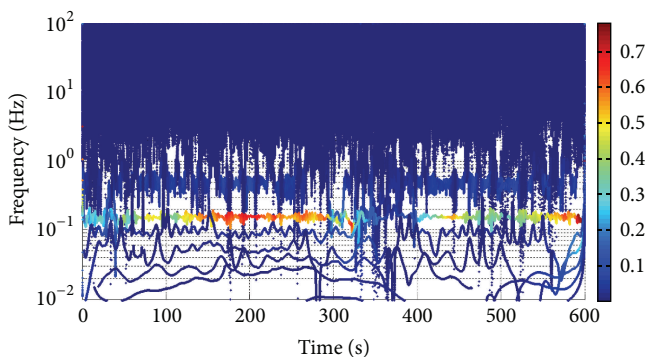

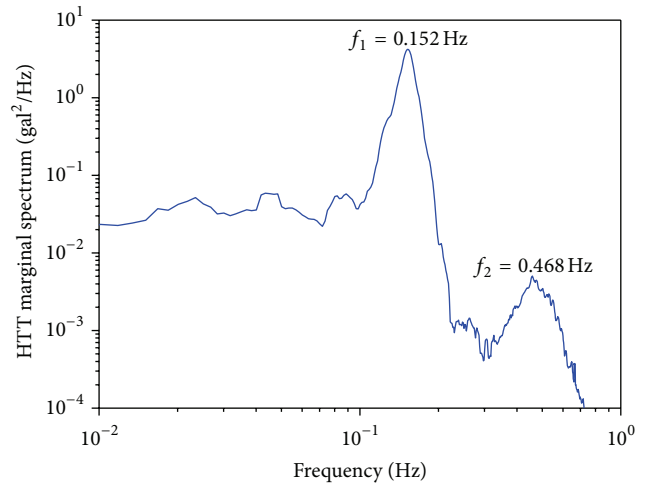FIGURE 26: Time-frequency analysis of field measured accelerations.

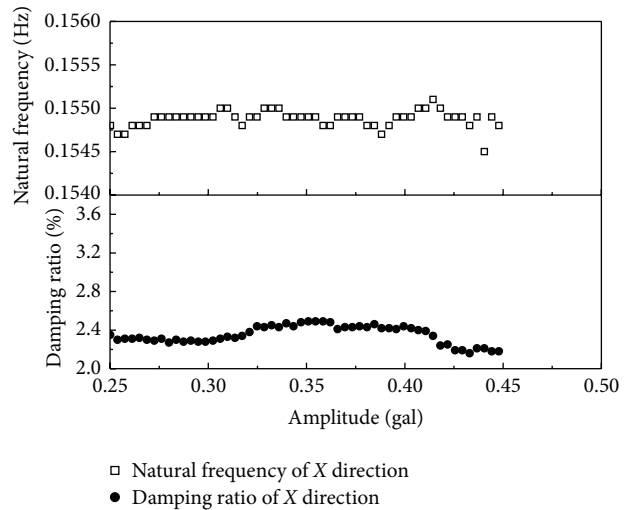FIGURE 27: Hilbert-Huang marginal spectra of field measured accelerations.

FIGURE 28: Natural frequencies and damping ratios versus amplitude in X direction.

(Figures 31 and 32). When the mean wind speeds are over 14.5 m/s, the field measured data in the Y direction (longitudinal direction) properly match the tested ones, while in the X direction (lateral direction) the field measured data are slightly larger than the tested ones. The differences between those two directions may be related to three issues: the difference of the wind directions, lateral aerodynamic damping, and the interference effects from surrounding buildings. Firstly, the wind angles corresponding to the measured data are variable within the interval of 107° to 170°, but the wind angle of the wind tunnel test is stable at 135° (Table 3). The wind-induced responses in the X direction (lateral direction) are sensitive to the wind direction changes; however, the longitudinal direction is a different case. Secondly, the calculation results of the wind tunnel are obtained by applying the aerodynamic force tested from the rigid model on the structural finite element model without
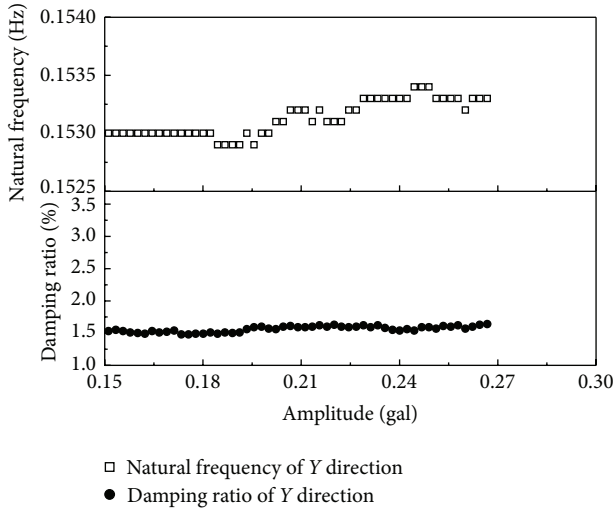
FIGURE 29: Natural frequencies and damping ratios versus amplitude in Y direction.
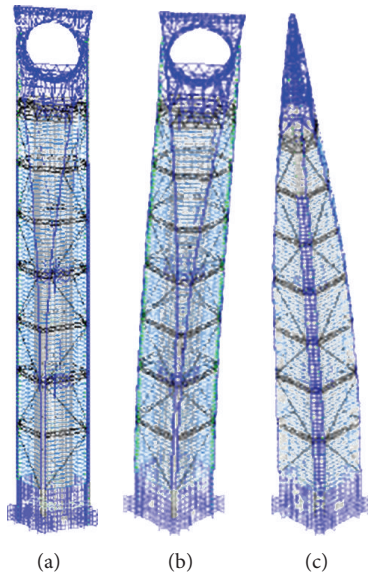

FIGURE 30: Finite element model and the first two bending modes: (a) finite element model, (b) basic bending mode in Y direction and (c) basic bending mode in X direction.

FIGURE 31: Tested wind-induced accelerations versus field measured ones in X direction.
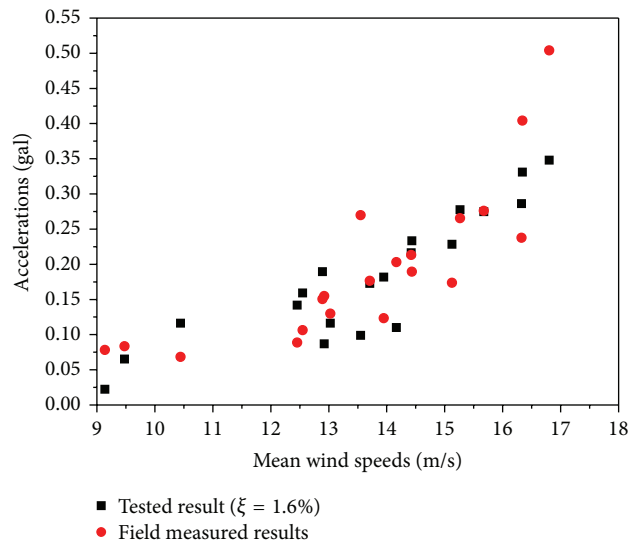
FIGURE 32: Tested wind-induced accelerations versus field measured ones in Y direction.

considering effects of the aerodynamic damping, whereas the lateral aerodynamic damping of this real super-tall building may be shown as a negative value [27]. Last, numerous differences also exist between the current surroundings and the wind tunnel test case.

6. Conclusions

Detailed analysis of the wind velocities at 500 m upper air in Shanghai and wind-induced responses of the SWFC under normal climate conditions is conducted by collecting data through the SHMS at the top of this building. The field measured results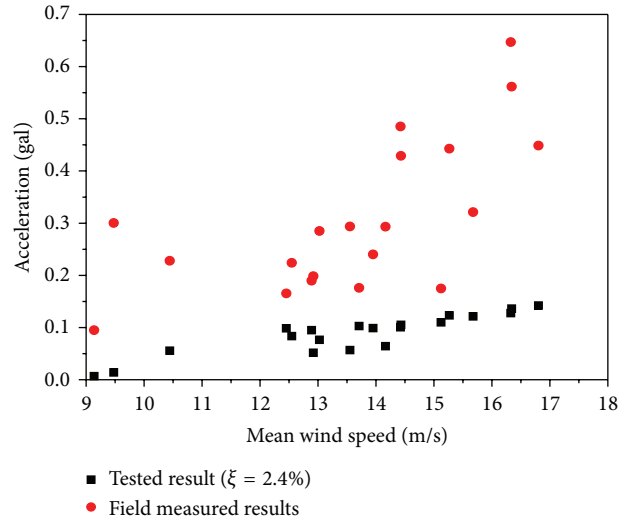 of the wind-induced responses are compared with the corresponding HFFB wind tunnel test results. The following conclusions are drawn.

(1) Through linear fitting, the ratio of maximum 10 min mean wind speeds within 1 hr and the 1 hr mean speed is approximately 1 : 1.04. The relationship between the maximum 3 s mean wind speeds within 10 min and the 10 min mean wind speeds is expressed as $y = 0.85x + 4.5$.

(2) When mean speed is small, both the turbulence intensity and the gust factor decrease with the increase of the mean wind speed. When the mean wind speed is over 20 m/s, the turbulence intensity and the gust factor are not sensitive to the changes of the mean

TABLE 3: 10 min mean wind speeds and mean wind angles for comparison during each period.

Date/time to record	10 min mean wind speed (m/s)	10 min mean wind angle (/°)
20101020/12:59:51	9.14	132.74
20101020/13:59:51	10.44	135.58
20101020/14:59:51	9.48	138.64
20101023/8:59:51	12.46	107.27
20101023/9:59:51	13.71	116.32
20101023/10:59:51	13.95	118.89
20101023/11:59:51	15.13	120.64
20101023/12:59:51	14.43	129.88
20101023/13:59:51	15.68	126.54
20101023/14:59:51	15.27	131.66
20101023/15:59:50	16.34	131.93
20101023/16:59:51	16.80	130.64
20101024/5:59:51	12.55	127.54
20101024/6:59:51	14.42	125.99
20101024/7:59:51	16.33	122.87
20101024/8:59:51	12.89	134.52
20101025/4:59:51	13.55	171.76
20101025/5:59:51	12.92	175.38
20101025/6:59:51	14.17	168.48
20101025/7:59:51	13.03	162.92

wind speed. The ratio of the lateral and longitudinal turbulence intensities is approximately 0.88.

(3) The power spectral densities of the longitudinal and lateral fluctuating wind speeds match well with the von Karman spectra when the mean wind speed is small. However, when the mean wind speed is over 20 m/s, the power spectral densities are larger than the von Karman spectra.

(4) The longitudinal and lateral turbulence integral scales have an increasing trend with the increase of mean wind speed. The ratio of the longitudinal and lateral turbulence integral scale is approximately $1 : 0.8$.

(5) The natural frequencies of the first two modes identified by using the power spectral density, HHT marginal spectra, and RDM match properly with the results from the finite element method. The damping ratio in X and Y directions is about 2.4% and 1.6%, respectively.

(6) The measured longitudinal and lateral responses match properly with the results from the wind tunnel test when the mean wind speeds are small. When the mean wind speed is over 20 m/s, the longitudinal responses of measurement and test match each other well, while the measured lateral responses are slightly larger than the tested ones. This phenomenon may be related to the differences of the approaching wind directions, lateral aerodynamic damping, and the building surroundings.

References

[1] C. S. Durst, "Wind speeds over short periods of time," *The Meteorological Magazine*, vol. 89, no. 1056, pp. 181–186, 1960.

[2] E. C. C. Choi, "Field measurement and experimental study of wind speed profile during thunderstorms," *Journal of Wind Engineering and Industrial Aerodynamics*, vol. 92, no. 3-4, pp. 275–290, 2004.

[3] N. Kato, T. Ohkuma, J. R. Kim, H. Marukawa, and Y. Niihori, "Full scale measurements of wind velocity in two urban areas using an ultrasonic anemometer," *Journal of Wind Engineering and Industrial Aerodynamics*, vol. 41, no. 1–3, pp. 67–78, 1992.

[4] J. D. McClintock, G. S. Pond, L. W. Davidson, Offshore Wind Gust Climatologies, and Sea Consult Limited, "Report prepared for atmospheric environment," Tech. Rep., Service Canadian Climate Center Marine Applied Unit, 1987.

[5] J. A. Wills, A. Grant, C. F. Boyack, Offshore Mean Wind Profile, and Department of Energy, "Offshore technical report," Tech. Rep. OTH86226, 1986.

[6] O. J. Andersen and J. Løvseth, "Gale force maritime wind. the Frøya data base. Part 1: sites and instrumentation. review of the data base," *Journal of Wind Engineering and Industrial Aerodynamics*, vol. 57, no. 1, pp. 97–109, 1995.

[7] O. J. Andersen and J. Løvseth, "Stability modifications of the Frøya wind spectrum," *Journal of Wind Engineering and Industrial Aerodynamics*, vol. 98, no. 4-5, pp. 236–242, 2010.

[8] Y. An, Y. Quan, and M. Gu, "Field measurement of wind characteristics of Typhoon Muifa on the Shanghai world financial center," *International Journal of Distributed Sensor Networks*, vol. 2012, Article ID 893739, 11 pages, 2012.

[9] G. L. Larose, A. Zasso, S. Melelli, and D. Casanova, "Field measurements of the wind-induced response of a 254 m high free-standing bridge pylon," *Journal of Wind Engineering and Industrial Aerodynamics*, vol. 74–76, pp. 891–902, 1998.

[10] Q. S. Li, J. R. Wu, S. G. Liang, Y. Q. Xiao, and C. K. Wong, "Full-scale measurements and numerical evaluation of wind-induced vibration of a 63-story reinforced concrete tall building," *Engineering Structures*, vol. 26, no. 12, pp. 1779–1794, 2004.

[11] Y. L. Xu and S. Zhan, "Field measurements of Di Wang Tower during Typhoon York," *Journal of Wind Engineering and Industrial Aerodynamics*, vol. 89, no. 1, pp. 73–93, 2001.

[12] Q. S. Li, Y. Q. Xiao, J. Y. Fu, and Z. N. Li, "Full-scale measurements of wind effects on the Jin Mao building," *Journal of Wind Engineering and Industrial Aerodynamics*, vol. 95, no. 6, pp. 445–466, 2007.

[13] J. Y. Fu, Q. S. Li, J. R. Wu, Y. Q. Xiao, and L. L. Song, "Field measurements of boundary layer wind characteristics and wind-induced responses of super-tall buildings," *Journal of Wind Engineering and Industrial Aerodynamics*, vol. 96, no. 8-9, pp. 1332–1358, 2008.

[14] J. Y. Fu, J. R. Wu, A. Xu, Q. S. Li, and Y. Q. Xiao, "Full-scale measurements of wind effects on Guangzhou West Tower," *Engineering Structures*, vol. 35, pp. 120–139, 2012.

[15] H. F. Bai, T. H. Yi, H. N. Li, and L. Ren, "Multisensors on-site monitoring and characteristic analysis of UHV transmission tower," *International Journal of Distributed Sensor Networks*, vol. 2012, Article ID 545148, 10 pages, 2012.

[16] T.-H. Yi, H.-N. Li, and M. Gu, "Recent research and applications of GPS-based monitoring technology for high-rise structures," *Structural Control and Health Monitoring*, vol. 20, no. 5, pp. 649–670, 2013.

[17] H.-N. Li, T.-H. Yi, X.-D. Yi, and G.-X. Wang, "Measurement and analysis of wind-induced response of tall building based on GPS technology," *Advances in Structural Engineering*, vol. 10, no. 1, pp. 83–93, 2007.

[18] "AIJ-RLB-2004 Recommendations for loads on buildings," Architecture Institute of Japan, Tokyo, Japan, 2004.

[19] "GB 50009-2012 Load code for the design of building structures," Architecture & Building Press, Beijing, China, 2012.

[20] S. Cao, Y. Tamura, N. Kikuchi, M. Saito, I. Nakayama, and Y. Matsuzaki, "Wind characteristics of a strong typhoon," *Journal of Wind Engineering and Industrial Aerodynamics*, vol. 97, no. 1, pp. 11–21, 2009.

[21] E. C. C. Choi, *Wind Loading in Hong Kong: Commentary on the Code of Practice on Wind Effects Hong Kong*, Hong Kong Institute of Engineers, Hong Kong, China, 1983.

[22] N. E. Huang, Z. Shen, R. L. Steven et al., "The empirical mode decomposition and the Hubert spectrum for nonlinear and non-stationary time series analysis," *Proceedings of the Royal Society A*, vol. 454, no. 1971, pp. 903–995, 1998.

[23] Y. Tamura, H. Yasui, and H. Marukawa, "Non-elastic responses of tall steel buildings subjected to across-wind forces," *Wind and Structures*, vol. 4, no. 2, pp. 147–162, 2001.

[24] X.-J. Hong and M. Gu, "Probability model and solution on earthquake effects combination in along wind resistant design of tall-flexible buildings," *Applied Mathematics and Mechanics*, vol. 27, no. 5, pp. 627–636, 2006.

[25] Report of SWFC Seismic Review, Mori Building Architects & Engineers (MORI), Tokyo, Japan, 2003.

[26] Wind Engineering Studies for the Shanghai World Financial Center, *PRC, (Part 1 Studies Accelerations and Torsion Velocities From Force Balance Studies Using Standard BLWTL Statistical Methodology)*, The University of Western Ontario, Ontario, Canada, 2002, BLWT-SS41-2002.

[27] A. G. Davenport, "The influence of turbulence on the aeroelastic responses of tall structures to wind," in *Practical Experiences with Flow-Induced Vibrations*, pp. 681–695, Springer, Karlsruhe, Germany, 1979.